J. Fluid Mech. (2013), *vol.* 716, *pp.* 83–95. © Cambridge University Press 2013
doi:10.1017/jfm.2012.510

Turbulent drag reduction using fluid spheres

J. J. J. Gillissen†

Department of Chemical Engineering, Delft University of Technology, Julianalaan 136, 2628 BL Delft, The Netherlands

(Received 20 July 2011; revised 8 October 2012; accepted 11 October 2012)

Using direct numerical simulations of turbulent Couette flow, we predict drag reduction in suspensions of neutrally buoyant fluid spheres, of diameter larger than the Kolmogorov length scale. The velocity fluctuations are enhanced in the streamwise direction, and reduced in the cross-stream directions, which is similar to the more studied case of drag reduction using polymers. Despite these similarities, the drag reduction mechanism is found to originate in the logarithmic region, while the buffer region contributes to a slight drag increase, which is opposite to polymer-induced drag reduction. Another striking difference is the reduction of the turbulent energy at the large scales and an enhancement at the small scales.

Key words: drag reduction, multiphase and particle-laden flows, turbulent boundary layers

1. Introduction

It is well-known that the drag of a turbulent boundary layer can be reduced by the addition of particles. A key property of a drag-reducing particle is a slender shape, a property which is shared by linear polymers (Virk 1975), macroscopic fibres (McComb & Chan 1985), micelles formed by surfactant (Warholic, Scmhidt & Hanratty 1999*b*) and worm-like agglomerates formed by charged clay particles (Gust 1976). Drag reduction is also observed for spherical solid particles in the gas phase (Rashidi, Hetsroni & Banerjee 1990) and for (nearly) spherical gas bubbles in the liquid phase (Madavan, Deutsch & Merkle 1985).

Drag reduction by slender particles is related to the orientation of the particles and the associated dissipation induced by the particles. Close to the wall, the particles align along the streamlines and do not generate dissipation. Away from the wall, the particles induce dissipative forces, that dampen the turbulent eddies, while leaving the shear in the viscous sublayer intact. This results in a thickening of the viscous sublayer, with the net effect of a reduced friction factor (Lumley 1973). Benzi *et al.* (2005) used these ideas to formulate a model for drag reduction based on the Reynolds-averaged momentum and energy equations, and a similar approach was later used by Iaccarino, Shaqfeh & Dubief (2010). In these models the effect of the drag-reducing polymers is incorporated by means of an effective viscosity, which is negligible at the wall and which increases with the wall distance. The validity of this viscosity model was demonstrated by direct numerical simulations, in which drag reduction was achieved by adding a wall-distance-dependent viscosity to the governing equations (De Angelis *et al.* 2004; Gillissen *et al.* 2007).

† Email address for correspondence: j.j.j.gillissen@tudelft.nl

https://doi.org/10.1017/jfm.2012.510 Published online by Cambridge University Press

In contrast to slender particles, the drag-reduction mechanism is poorly understood for spherical additives, such as solid particles or gas bubbles. Mechanistic speculations for drag reduction induced by solid particles are based on the density contrast between the particles and the suspending gas. As an effect the particle response time is large compared to the characteristic time of the near-wall vortices, even when the particles are smaller than the Kolmogorov length scale. The heavy particles, that do not follow the rapid motions of the near-wall vortices, generate forces that dampen these vortices (Zhao, Andersson & Gillissen 2010). In liquids on the other hand, sub-Kolmogorov spheres have negligible response times and merely induce an increase in the apparent suspension viscosity, leading to an enhancement of the overall drag. In order for non-trivial effects to occur in liquid suspensions of spheres, the spheres need to be large compared to the turbulent eddies.

For gas bubbles, several speculations on the drag-reduction mechanism have been put forward. Lu, Fernández & Tryggvason (2005) argue that the gas bubbles deform into a shape that 'squeezes' the coherent, near-wall vortices. According to Xu, Maxey & Karniadakis (2002) the large density contrast drives the bubbles to high-vorticity regions, effectively destroying the near-wall vortices. In this work we show that neither deformability nor density contrast is a requisite for drag reduction with spheres. For this purpose we numerically simulate drag reduction in turbulent Couette flow using suspensions of neutrally buoyant, fluid spheres.

2. Governing equations and numerical method

2.1. *Fluid motion*

We consider suspensions of neutrally buoyant fluid spheres of radius R, with the same mass density and the same viscosity as the suspending liquid. The volume fraction of the spheres is denoted Φ. The fluid spheres can be conceived as non-coalescing liquid droplets, with a very large surface tension. Numerically we describe the problem by one flow field that governs both the suspending liquid phase and the dispersed droplet phase. On the droplet interface, the normal fluid velocity is restricted by the no-penetration condition, while the tangential velocity is free to evolve. The flow is computed in a three-dimensional domain, which is bounded by two walls at $y = 0$ and $y = H$, which move in opposite directions with velocities $\pm U_W$ along the x-axis, as sketched in figure 1. The suspending liquid and the spheres are subjected to periodic boundary conditions in the x- and z-directions, while at $y = 0$ and at $y = H$ the fluid obeys the no-slip condition and the spheres reflect specularly. Fully elastic, hard-sphere collisions prevent overlap between the spheres and between the spheres and the walls (Chen, Kontomaris & McLaughlin 1998).

We solve the hydrodynamics with our in-house lattice-Boltzmann (LB) code (Gillissen, Sundaresan & Van Den Akker 2011). In the limits of low Knudsen number and low Mach number the LB method mimics the continuity equation:

$$\frac{\partial \rho}{\partial t} + (\boldsymbol{\nabla} \cdot \rho \boldsymbol{u}) = 0, \tag{2.1a}$$

and the Navier–Stokes equation (Wolf-Gladrow 2000):

$$\rho \left(\frac{\partial \boldsymbol{u}}{\partial t} + \boldsymbol{u} \cdot \boldsymbol{\nabla} \boldsymbol{u} \right) = \boldsymbol{\nabla} \cdot (-p\boldsymbol{\delta} + 2\mu \boldsymbol{S}) + \boldsymbol{F}, \tag{2.1b}$$

where t is time, ρ is the fluid mass density, $\boldsymbol{u}$ is the liquid velocity, p is the fluid pressure, $\boldsymbol{S} = (1/2)[(\boldsymbol{\nabla u})^{\mathrm{T}} + \boldsymbol{\nabla u}]$ is the rate of strain tensor, ν is the kinematic

https://doi.org/10.1017/jfm.2012.510 Published online by Cambridge University Press

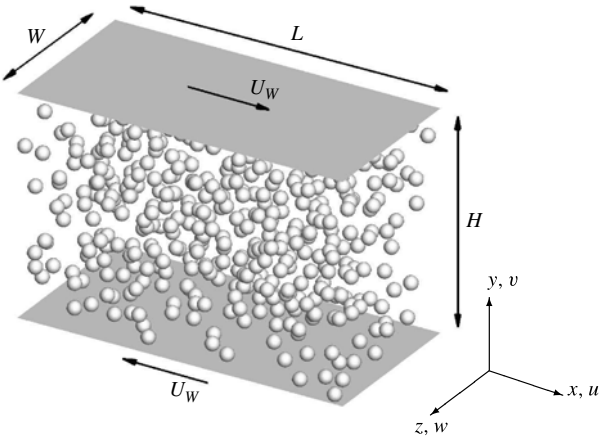


FIGURE 1. Sketch of the computational setup.

viscosity, $\mu = \rho\nu$ is the dynamic viscosity, $\boldsymbol{\nabla}$ is the nabla operator, $\boldsymbol{\delta}$ is the unit tensor and $\boldsymbol{F}$ is a force field to ensure the no-penetration condition on the spheres, discussed in § 2.2. Equation (2.1) describes the fluid flow inside the continuous phase as well as in the spheres.

We use u, v and w to denote the x-, y- and z-components of the velocity vector $\boldsymbol{u}$. According to the Reynolds decomposition we use $\overline{u}$ and u' to denote the mean and the fluctuation part of a variable u and we use u_{rms} to denote its standard deviation, where the Reynolds average $\overline{\cdots}$ is the average over time and over the homogeneous coordinates (x and z), spanning both the continuous and discontinuous phases. Variables indicated by a superscript $+$ are given in wall units, which means that they are scaled with the mass density ρ, the kinematic viscosity ν and the friction velocity $U_\tau = \sqrt{\tau_W/\rho}$, where τ_W denotes the wall shear stress. It is noted that in the LB method there are small density fluctuations. We use the Reynolds-averaged fluid density at the wall as the characteristic density scale ρ. For all flow simulations reported in this article we verified that the fluctuations in the mass density were $<0.5\,\%$, such that deviations from incompressibility, inherent in the LB method, can be ignored.

The grid cells used in the present study are cubic and of uniform size. Uniform grids are well-suited for resolving spherical particles. However they require more grid points compared to refined grids. Refined grids are therefore more suited for calculations of single-phase turbulent boundary layers, such as Pasinato (2011).

2.2. *Immersed boundary method*

The no-penetration condition on the surface S of the spheres is enforced using an immersed boundary method. The method involves the addition of a force field $\boldsymbol{F}$ to (2.1*b*) that is localized around S and that drives the fluid velocity at S to the no-penetration velocity.

The force field is constructed by means of N control points per sphere, which are distributed equidistantly over S. The fluid velocity on these control points is interpolated from the fluid velocities on the neighbouring grid points. On each control point a force is computed that counteracts the normal component of the difference between the interpolated fluid velocity and the sphere velocity. This force is then distributed to the neighbouring grid points.

https://doi.org/10.1017/jfm.2012.510 Published online by Cambridge University Press

The force field takes the following form:

$$\boldsymbol{F}(\boldsymbol{x}) = \sum_{\alpha=1}^{N} \boldsymbol{F}_\alpha \delta\left(\boldsymbol{x} - \boldsymbol{y}_\alpha\right), \quad \boldsymbol{F}_\alpha = \frac{\Delta S \rho_\alpha}{\Delta t \Delta x^2} \left(\boldsymbol{u}_P - \boldsymbol{u}_\alpha\right) \cdot \boldsymbol{n}_\alpha \boldsymbol{n}_\alpha. \tag{2.2}$$

Here $\boldsymbol{F}_\alpha$ is the no-slip force due to control α which is located at position $\boldsymbol{y}_\alpha$, ρ_α is the interpolated fluid density at control point α, $\boldsymbol{u}_\alpha$ is the interpolated fluid velocity at control point α, $\boldsymbol{n}_\alpha$ is the normal on the sphere at control point α, $\boldsymbol{u}_P$ is the particle translational velocity, $\delta(x)$ is a reguralized delta-function, which is smoothed over three grid cells Δx (Uhlmann 2005) and ΔS is the surface area corresponding to a single control point $\Delta S = 4\pi R^2/N$. In the present work we have used $\Delta S/\Delta x^2 = 0.5$. We found that in the range $\Delta S/\Delta x^2 < 0.7$ the numerical results do not depend on the value of ΔS.

The immersed boundary force $\boldsymbol{F}$ is also used to compute the translation of the spheres. The corresponding equation of motion is derived in appendix A. It is noted that since the force field $\boldsymbol{F}$ is normal to S, it does not impose torques and therefore it does not affect the rotation of the spheres. The rotation is governed by the fluid equations of motion which are solved over the whole domain, including the volume of the spheres.

3. Validation

3.1. *Laminar two-phase flow*

The numerical method is validated by computing the shear stress in a low-Reynolds-number Couette flow of a suspension of fluid spheres. In the limit of vanishing Reynolds number $Re_p = U_W R^2/\nu H \ll 1$, vanishing volume fraction $\Phi \ll 1$ and vanishing wall effects $R/H \ll 1$, Taylor (1932) derived that the shear stress in the suspension is $\tau = \mu(1 + (7/4)\Phi)\,\mathrm{d}\overline{u}/\mathrm{d}y$, where $\overline{u}$ is the Reynolds-averaged velocity.

To verify this relation we conduct simulations using $\Phi = 0.0125$, 0.025, 0.05 and 0.1, and $Re_p = 0.1$ and $R/H = 0.045$, corresponding to 29, 58, 116 and 232 spheres in the cubic domain. To study the dependence of the numerical accuracy on the grid resolution, we conducted three sets of simulations on three different cubic grids composed of 96^3, 128^3 and 192^3 grid points, corresponding to a grid resolution per sphere radius of $R/\Delta x = 4.5$, 6 and 9. The time step for the three simulation sets was chosen such that $\Delta t U_W/\Delta x = 0.024$, 0.018 and 0.012, respectively.

Figure 2(*c*) shows the fractional increase in the effective viscosity due to the presence of the spheres $\mu_{eff}/\mu = \tau/(\mu\,\mathrm{d}\overline{u}/\mathrm{d}y)$ as a function of the volume fraction $\tilde{\phi}$. The plotted values for the volume fraction $\tilde{\phi}$ and μ_{eff} are averaged over $0.25 < y/H < 0.75$, as exemplified for the $(\Phi = 0.1; R/\Delta x = 4.5)$ case by the dashed lines in figure 2(*a,b*). Note that $\tilde{\phi}$ is close to but not equal to the volume averaged volume fraction Φ. The Reynolds-averaged volume fraction in figure 2(*a*) is computed as $\overline{\phi} = 1 - \overline{\Psi}$, where Ψ is a marker function, which is zero in the spheres and one in the suspending liquid. The simulation results in figure 2(*c*) agree well with the theory of Taylor (1932) and the accuracy increases with increasing grid resolution.

3.2. *Turbulent single-phase flow*

We further validate the numerical method for single-phase turbulent Couette flow on a $(192 \times 128 \times 96)$-grid and a $(1.5H \times H \times 0.75H)$-domain in the x-, y- and z-directions. The Reynolds number based on the full channel height H and the velocity difference

https://doi.org/10.1017/jfm.2012.510 Published online by Cambridge University Press

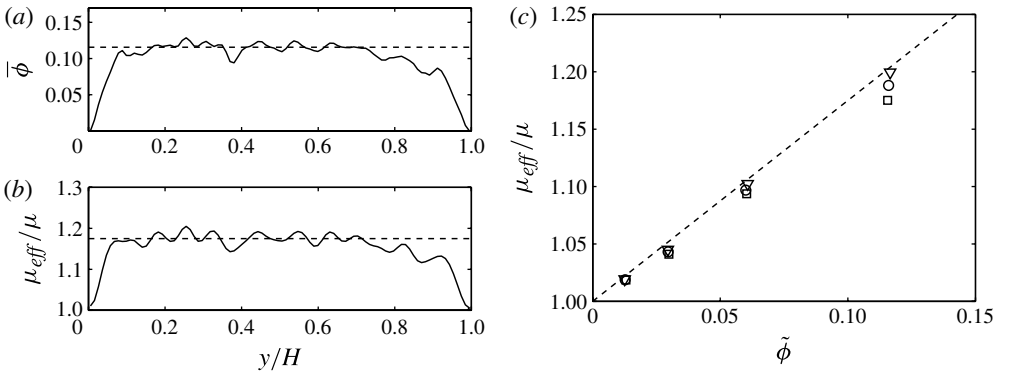


FIGURE 2. (*a*) Reynolds-averaged volume fraction and (*b*) scaled effective viscosity $\mu_{eff}/\mu = \tau/(\mu\, \mathrm{d}\overline{u}/\mathrm{d}y)$ versus wall distance, for a simulation where the volume-averaged volume fraction is $\Phi = 0.1$ and the grid resolution is $R/\Delta x = 4.5$. The dashed lines correspond to the averaged values between $y/H = 0.25$ and $y/H = 0.75$. (*c*) Scaled effective viscosity versus volume fraction for simulations using $R/\Delta x = 4.5$ (squares), $R/\Delta x = 6.0$ (circles), $R/\Delta x = 9.0$ (triangles) and Taylor's relation $\mu_{eff}/\mu = 1 + (7/4)\Phi$ (dashed line).

between the two walls $2U_W$ equals $Re = H2U_W/\nu = 13\,307$. The Reynolds number based on H and the friction velocity U_τ equals $Re_\tau = HU_\tau/\nu \approx 360$. These parameters are identical to the ones used in the suspension simulation, reported in § 4. The non-dimensional grid size is $\Delta y^+ \approx 2.8$ and the streamwise and spanwise domain sizes are $L^+ \approx 540$ and $W^+ \approx 270$. The time step equals $\Delta t U_W/\Delta x = 0.1$, which ensures a sufficiently low Mach number, such that the LB method accurately approximates the incompressible Navier–Stokes equations.

As initial conditions for the velocity field we use the law of the wall plus random fluctuations with an amplitude of $5U_\tau$. The law of the wall is the theoretical mean velocity profile in the turbulent boundary layer: $(\overline{u} - U_W)^+ = y^+$ for $y^+ < 11.6$ and $(\overline{u} - U_W)^+ = 2.5 \log y^+ + 5.5$ for $y^+ > 11.6$. After starting the simulation we monitored the total kinetic energy and the friction factor $f = (U_\tau/U_W)^2$, revealing an initial transient phase of $t^+ \approx 3000$, before reaching fully developed turbulence, after which statistics were collected from 2000 samples equidistantly distributed over a period of $t^+ \approx 10\,000$. We ascertained that we sampled over a sufficiently large time interval by verifying that the total shear stress τ did not vary more than 1 % as a function of y, which is by definition constant in fully developed Couette flow.

We compare our results to the results of Pasinato (2011), who discretized the incompressible Navier–Stokes equations, using a finite-difference method. They use a similar Reynolds number $Re = H2U_W/\nu \approx 10\,000$ on a $(7\pi H \times H \times 5\pi H/4)$ domain which is much larger than our domain. Their refined $(128 \times 128 \times 128)$-grid, has a wall-normal grid spacing at the wall of $\Delta y^+ \approx 0.2$, which is sufficiently small to resolve the steep velocity gradient in the viscous sublayer. Their streamwise and spanwise domain sizes $L^+ \approx 6600$ and $W^+ \approx 1200$, are large enough to capture not only the near-wall, vortical structures, but also the large, central structures (Komminaho, Lundbladh & Johansson 1996).

In figure 3 we compare our simulated mean flow $\overline{u}$, relative to the wall, the Reynolds shear stress $-\overline{uv}$, the viscous shear stress $\mathrm{d}\overline{u}/\mathrm{d}y$ and the standard deviation of the components of the fluid velocity vector $\boldsymbol{u}_{rms}$ to the data of Pasinato (2011). Owing to symmetry we only show half of the channel. The channel wall and the

https://doi.org/10.1017/jfm.2012.510 Published online by Cambridge University Press

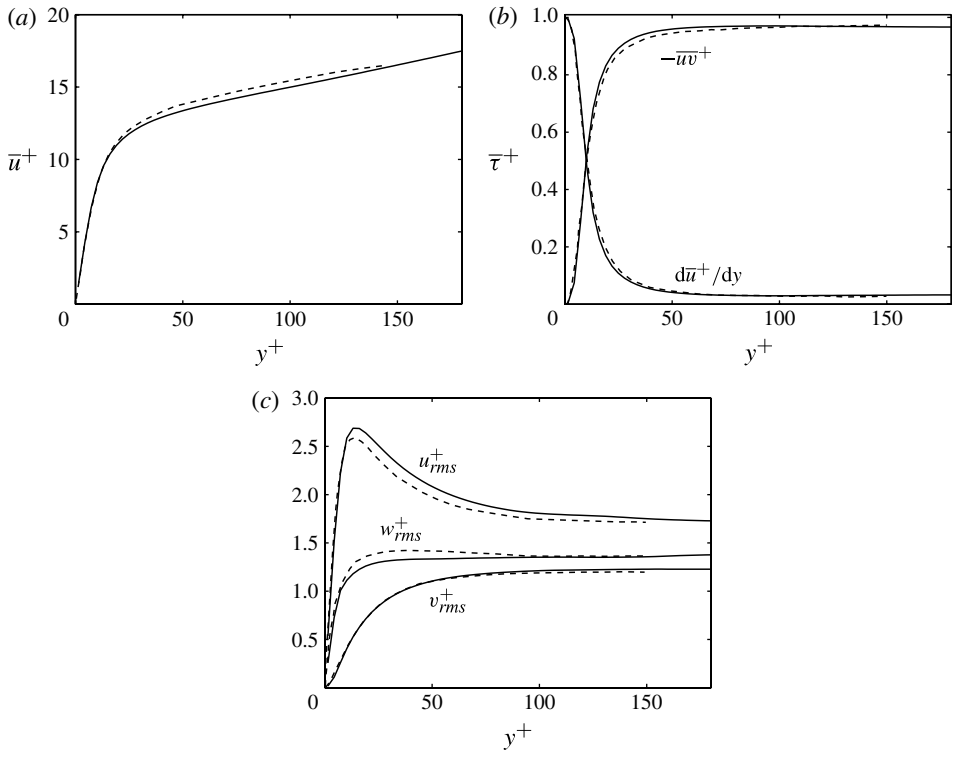


FIGURE 3. (*a*) Mean flow $\overline{u}$, (*b*) Reynolds stress $-\overline{uv}$ and viscous stress $\mathrm{d}\overline{u}/\mathrm{d}y$ and (*c*) standard deviation of the fluid velocity $\boldsymbol{u}_{rms}$ versus wall distance y, in wall units. Comparison between present simulation (solid lines) and the simulation of Pasinato (2011) (dashed lines).

channel centreline are located at $y^+ = 0$ and $y^+ \approx 180$, respectively. The simulation data match the data of Pasinato (2011) within a few per cent. This agreement implies that our streamwise and spanwise dimensions are sufficiently large, and our grid spacing is sufficiently small for obtaining reliable statistics, including an accurate representation of the velocity profile in the viscous sublayer.

4. Drag reduction

4.1. *Parameters*

We use the following parameters in the simulation of the turbulent Couette flow of a suspension of fluid spheres. The Reynolds number is $Re = 2U_W H/\nu = 13\,307$. The mass density of the spheres is equal to the fluid mass density ρ, and the volume-averaged volume fraction of the spheres is $\Phi = 0.125$, corresponding to 326 spheres. Per sphere we use around 9.0×10^2 control points in the immersed boundary method, to satisfy the no-penetration condition on the spheres. The sphere radius is $R/H \approx 0.047$, corresponding to $R/\Delta x = 6$ grid points per radius.

In § 3.1 we studied the accuracy of the code in predicting the shear stress generated by fluid spheres, in low-Reynolds-number sheared suspensions. At this particular volume fraction and grid resolution, we found a 5 % discrepancy in this shear stress with the corresponding theoretical prediction; see figure 2(*c*).

https://doi.org/10.1017/jfm.2012.510 Published online by Cambridge University Press

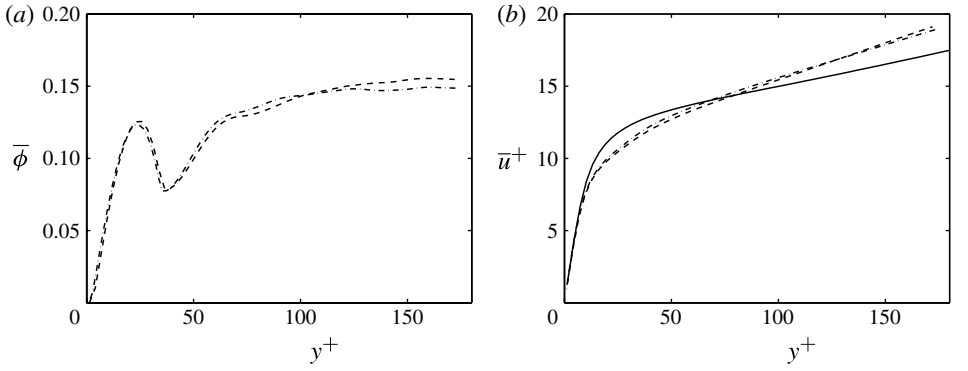


FIGURE 4. (*a*) Particle volume fraction ϕ and (*b*) suspension velocity $\overline{u}$ versus wall distance y for $\Phi = 0$ (solid lines), $\Phi = 0.125$ (dashed lines) and $\Phi = 0.125$ on a finer mesh (dash-dotted lines).

To keep the computations within feasible limits, we use a relatively small domain of $(1.5H \times H \times 0.75H)$, with a grid resolution of $(192 \times 128 \times 96)$. A Newtonian reference case without spheres has also been computed using the same parameters.

In § 3.2 we showed that with these domain sizes and grid resolutions, the first- and second-order fluid velocity statistics are within a few per cent of those obtained on a larger domain and a finer grid, in the wall-normal direction. Higher-order statistics might deviate, but since our main interest is the behaviour of the drag, the benefits of using a small domain outweigh the possible discrepancies in the higher-order statistics.

4.2. *Particle concentration*

The Reynolds-averaged volume fraction $\overline{\phi}$ is plotted as a function of the distance to the wall y in figure 4(*a*). Since the particle centre cannot approach the wall within a distance R, the $\overline{\phi}$-profile falls to zero for $y < R$. A layer of particles is formed next to the wall, reflected by the extrema in the $\overline{\phi}$-profile, with a maximum and a minimum located at $y^+ \approx R^+ \approx 17$ and $y^+ \approx 2R^+ \approx 34$, respectively.

4.3. *Drag reduction*

Figure 4(*b*) shows the Reynolds-averaged suspension velocity $\overline{u}$, relative to the wall velocity, which is obtained by averaging over both the continuous and the discontinuous phases. The scaled centreline velocity, $U_C^+ = \overline{u}^+$ at $y^+ \approx 180$, is related to the friction factor f by $U_C^+ = f^{-1/2}$. The increase of U_C^+ in the suspension compared to the Newtonian flow corresponds to a 15 % reduction in the friction factor. Figure 4(*b*) shows that in the drag-reduced flow there is an increase in the slope of the logarithmic profile. This is different with polymer-induced drag-reduced flow, which shows a parallel upward shift of the logarithmic profile; see e.g. Warholic, Massah & Hanratty (1999*a*).

4.4. *Grid resolution*

The particle radius equals $R^+ \approx 17$ which corresponds to 12 grid points per particle diameter. To demonstrate the adequacy of the numerical grid to resolve the fluid flow around the spheres, we have conducted an additional suspension simulation, using the same parameters as the ones described in § 4.1, except for a 1.5 increase

https://doi.org/10.1017/jfm.2012.510 Published online by Cambridge University Press

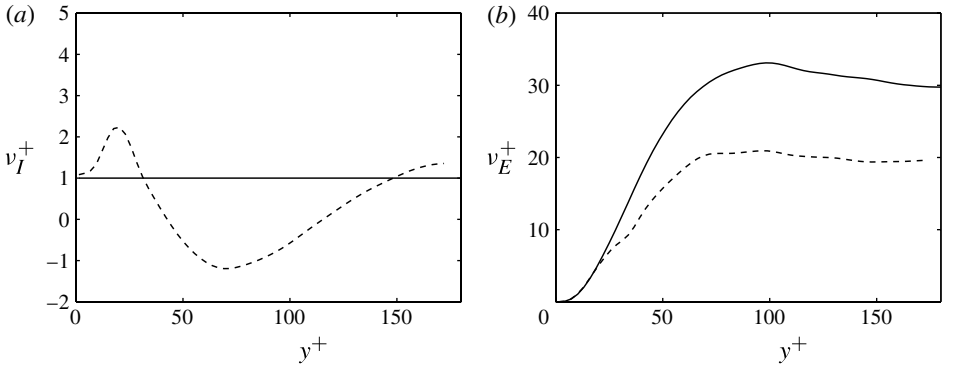


FIGURE 5. (*a*) Suspension internal viscosity ν_I and (*b*) suspension eddy viscosity ν_E versus wall distance y for $\Phi = 0$ (solid lines) and $\Phi = 0.125$ (dashed lines).

of grid points in each direction: (288 × 192 × 144), corresponding to 18 grid points per particle diameter. Figure 4 shows very good agreement in the profiles of the particle concentration and the mean flow, between the (192 × 128 × 96) grid and the (288 × 192 × 144) grid. This demonstrates the adequacy of the (192 × 128 × 96) grid in correctly capturing the drag-reduction phenomenon. In the remainder of the paper, we present results obtained from the simulation on the (192 × 128 × 96) grid.

4.5. *Shear stress budgets*

To shed light on the drag-reduction mechanism, we analyse the different components in the shear stress balance, which states that the shear stress τ is independent of the wall distance. The shear stress can be decomposed into the liquid viscous stress τ_V, the liquid Reynolds stress τ_R, the particle surface stress τ_P and the particle momentum flux τ_M:

$$\tau = \tau_V + \tau_R + \tau_P + \tau_M. \tag{4.1}$$

Expressions for these terms are derived in appendix B. We lump the four shear stress components into two effective viscosities. The *suspension eddy viscosity* ν_E is based on τ_R and τ_M:

$$\nu_E = \frac{\overline{\tau}_R + \overline{\tau}_M}{\rho\, \mathrm{d}\overline{u}/\mathrm{d}y}, \tag{4.2a}$$

and the *suspension internal viscosity* ν_I is based on τ_V and τ_P:

$$\nu_I = \frac{\overline{\tau}_V + \overline{\tau}_P}{\rho\, \mathrm{d}\overline{u}/\mathrm{d}y}. \tag{4.2b}$$

Figure 5(*a*) shows the profiles of the internal viscosity ν_I. In the Newtonian flow $\nu_I = \nu$. The excess $\nu_I - \nu$ in the suspension is due to the no-penetration condition on the spheres. In contrast to polymers, where $\nu_I - \nu$ is approximately a linear function of y (Gillissen *et al.* 2007; Benzi *et al.* 2008), the excess viscosity $\nu_I - \nu$ in the suspension displays a rather complex, non-monotonic behaviour. Starting from zero at the wall, it first increases, passes through a maximum at the location of the maximum $\overline{\phi}$ (see figure 4*a*), then decreases, becomes negative and finally increases towards the channel

https://doi.org/10.1017/jfm.2012.510 Published online by Cambridge University Press

centreline. The negative $\nu_I - \nu$ values are remarkable. However in the corresponding region, ν_I contributes little to the total shear stress, i.e. the eddy viscosity ν_E, shown in figure 5(*b*), is an order of magnitude larger than ν_I.

At $y^+ \lessapprox 20$ on the other hand, ν_I dominates the shear stress, which could suggest that drag reduction originates in the buffer and viscous regions, similar to polymer solutions. However for $y^+ \lessapprox 20$, the increase in ν_I is larger than the reduction in ν_E, which means that this region contributes to a drag increase. Figure 5 shows that drag reduction originates from $y^+ \gtrapprox 20$, where the increase of ν_I is overwhelmed by the decreases of ν_E. This is fundamentally different from drag reduction induced by polymers, where, for relatively small levels of drag reduction $\lesssim 20\,\%$, the shear stress balance is modified only in the near-wall region $y^+ \lessapprox 20$, while it is more or less unaffected in the logarithmic region $y^+ \gtrapprox 20$.

For polymers, drag reduction can effectively be modelled by replacing the time- and space-dependent polymer stress by a *polymer viscosity*. The polymer viscosity is based on the Reynolds-averaged polymer stress, predicted by the full constitutive equations (Gillissen *et al.* 2007). To test this idea on spheres, we run a simulation without spheres, but with an additional viscosity instead. This viscosity is defined by the excess internal viscosity $\nu_I - \nu$ and taken from figure 5(*a*). The result showed a significant drag increase, demonstrating that, unlike the polymer stress, the stress induced by large spheres cannot be modelled by an effective viscosity profile. This observation further marks the contrast between the two drag-reduction mechanisms. Polymers act on the molecular scale, extending the viscous-dominated region into the buffer region. Large spheres, on the other hand, geometrically disrupt the momentum-transferring eddies in the inertial layer.

4.6. *Turbulence modulation*

Figure 6(*a*) compares the standard deviation of the components of the fluid velocity vector $\boldsymbol{u}_{rms}$ in the drag-reduced flow to those in the Newtonian flow. Away from the wall, $y^+ \gtrapprox 20$, the spheres enhance the streamwise velocity fluctuations u_{rms}, which is probably due to the larger turbulence-producing mean velocity gradient $\mathrm{d}\overline{u}/\mathrm{d}y$. Furthermore at $y^+ \gtrapprox 20$, the spheres act to reduce the wall-normal and the spanwise velocity fluctuations: v_{rms} and w_{rms}. The peak of u_{rms} is shifted outward, while its height is unchanged. Close to the wall, v_{rms} and w_{rms} are slightly enhanced. In polymer solutions there is an increase in the peak value of u_{rms}, while v_{rms} and w_{rms} are reduced everywhere, also close to the wall; see e.g. Warholic *et al.* (1999*a*). This further indicates the structural difference between the present type of drag reduction and polymer-induced drag reduction.

The difference is further exemplified in figure 6(*b*), which shows the power spectra of the streamwise velocity at $y^+ \approx 10$. The spectra reveal that the spheres enhance velocity fluctuations on the small scales, while they dampen the fluctuations on the large scales. These trends are opposite to those observed in polymer-induced drag reduction, see e.g. Warholic *et al.* (1999*a*).

The effect of the spheres on the structure of the turbulence is further illustrated in figure 6(*c*). This figure shows the two-point autocorrelation function of the streamwise velocity fluctuations C_{xx} along the x-axis, which is the Fourier transform of the power spectrum, shown in figure 6(*b*). In the suspension, C_{xx} decays faster to zero with x than in the Newtonian flow, which indicates a smaller eddy size in the presence of the spheres.

https://doi.org/10.1017/jfm.2012.510 Published online by Cambridge University Press

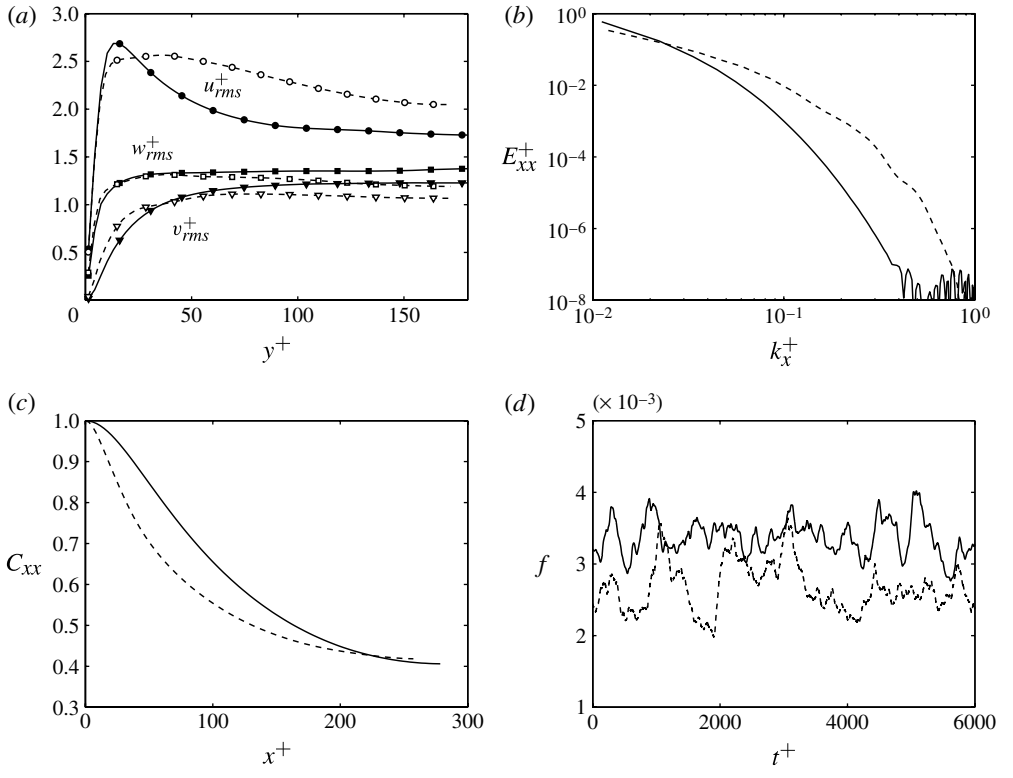


FIGURE 6. (*a*) Standard deviation of the fluid velocity vector $\boldsymbol{u}_{rms}$ versus the wall distance y. (*b*) Streamwise power spectrum of the streamwise velocity fluctuations E_{xx} at $y^+ \approx 10$. (*c*) Two-point autocorrelation function for the streamwise velocity fluctuations C_{xx} along the x-axis at $y^+ \approx 10$. (*d*) The friction factor f versus the time t. Solid line, $\Phi = 0$; dashed line, $\Phi = 0.125$.

It is noted that in our small domain, C_{xx} does not reach the uncorrelated value of zero. It is known that Couette flow requires a very large separation distance $x \gtrsim 10H$, for the fluctuations to become fully uncorrelated, see e.g. Komminaho *et al.* (1996). Owing to the use of cubic and homogeneous grids in the present numerical method, simulating on such large domains is unfeasible, requiring excessive amounts of grid nodes. However, we demonstrated in § 3.2 that our small domain size does not pose restrictions on the physics that is responsible for the friction factor, with correct profiles of the mean flow and the Reynolds stress. Since the correlation length is reduced, the domain size is probably even less restrictive in the presence of the spheres.

Finally we show in figure 6(*d*) the time evolution of the friction factor $f = \tau/\rho U_W^2$. In correspondence to figure 4(*b*), there is an average reduction of 15 % in the suspension drag, compared to the Newtonian flow. The figure also shows that this reduction is not linked to an enhanced intermittency or periods of re-laminarization, which occur in polymer-induced drag reduction, especially in simulations on small domains, see e.g. Xi & Graham (2010). Together with the observed reduction of the correlation length in figure 6(*c*), this further justifies the use of our small computational domain.

https://doi.org/10.1017/jfm.2012.510 Published online by Cambridge University Press

5. Conclusions

We have used lattice-Boltzmann and immersed boundary methods to simulate the turbulent Couette flow of a 12.5 % volume fraction suspension of neutrally buoyant fluid spheres, with a radius of $R^+ \approx 17$. The system showed a 15 % reduction in the friction factor.

The drag-reduction mechanism is compared to that of polymers. As opposed to polymer-induced drag reduction, the velocity slope in the buffer region is reduced, while the slope in the logarithmic region is enhanced. This reflects that the drag reduction originates in the logarithmic region, while the buffer region contributes to a slight drag increase. These trends are supported by an analysis of the various contributions to the shear stress balance.

Similar to polymer-induced drag reduction, the fluid velocity fluctuations are enhanced in the streamwise direction, and they are reduced in the cross-stream directions. Unlike the polymer case, the turbulent energy spectrum is enhanced at the small scales and it is suppressed at the large scales.

These observations mark the different drag-reduction mechanisms of large spheres and polymers. Owing to their small size polymers primarily act in the viscous sublayer, effectively stabilizing and thickening the buffer region. Large spheres on the other hand pose geometrical constraints on the eddies in the inertial region, disrupting their Reynolds stress.

Acknowledgements

This work was supported by Stichting Nationale Computerfaciliteiten (National Computing Facilities Foundation NCF) through the use of supercomputer facilities, with financial support from the Nederlandse Organisatie voor Wetenschappelijk Onderzoek (Netherlands Organization for Scientific Research, NWO). M. Yusuf is acknowledged for discussions.

Appendix A. Equation of motion of the fluid sphere

Without gravity Newton's equation of motion for a suspended fluid sphere reads

$$\rho V_P \boldsymbol{a}_P = -\int_S (p\boldsymbol{\delta} - 2\mu \boldsymbol{S}) \cdot \boldsymbol{n} \, \mathrm{d}S, \tag{A 1a}$$

where ρV_P is the particle mass and $\boldsymbol{a}_P$ is the particle acceleration. Integrating (2.1*b*) over the particle volume yields

$$\rho V_P \boldsymbol{a}_P = -\int_S (p\boldsymbol{\delta} - 2\mu \boldsymbol{S}) \cdot \boldsymbol{n} \, \mathrm{d}S + \frac{1}{2}\sum_{\alpha=1}^{N} \boldsymbol{F}_\alpha. \tag{A 1b}$$

The factor $1/2$ stems from the fact that half of the force field $\boldsymbol{F}$ is distributed to grid nodes inside the particle while the other half is distributed to nodes outside the particle. Combining (A1*a*) and (A1*b*) gives

$$\sum_{\alpha=1}^{N} \boldsymbol{F}_\alpha = \boldsymbol{0}. \tag{A 1c}$$

https://doi.org/10.1017/jfm.2012.510 Published online by Cambridge University Press

Combining (A1c) and (2.2) gives the following expression for the particle velocity:

$$\boldsymbol{u}_P = \frac{\sum_{\alpha=1}^{N} \rho_\alpha \boldsymbol{u}_\alpha \cdot \boldsymbol{n}_\alpha \boldsymbol{n}_\alpha}{\frac{1}{3}\sum_{\alpha=1}^{N} \rho_\alpha}, \tag{A 1d}$$

where we used that $\sum_{\alpha=1}^{N} \boldsymbol{n}_\alpha \boldsymbol{n}_\alpha \approx \boldsymbol{\delta}/3$.

Appendix B. Shear stress balance

The shear stress balance is derived by rewriting (2.1b) as follows:

$$\rho \frac{\partial \boldsymbol{u}}{\partial t} = \boldsymbol{\nabla} \cdot [-p\boldsymbol{\delta} - \rho \boldsymbol{u}\boldsymbol{u}\Psi + 2\mu \boldsymbol{S}\Psi - \rho \boldsymbol{u}\boldsymbol{u}\,(1-\Psi) + 2\mu \boldsymbol{S}\Psi\,(1-\Psi)] + \boldsymbol{F}. \tag{B 1a}$$

Here the marker function Ψ equals one in the liquid phase and it equals zero inside the spheres. Applying the Reynolds average $\overline{\cdots}$ to the x-component of this equation gives

$$\frac{\mathrm{d}}{\mathrm{d}y}\left[-\overline{\rho u_x u_y \Psi} + 2\overline{\mu S_{xy}\Psi} - \overline{\rho u_x u_y\,(1-\Psi)} + 2\overline{\mu S_{xy}\,(1-\Psi)}\right] + \overline{F_x} = 0, \tag{B 1b}$$

where it was used that Reynolds averages do not depend on t, x and z and that $\boldsymbol{\nabla}\bar{p} = \boldsymbol{0}$. The shear stress balance is obtained by integrating (B1b) from $y' = 0$ to $y' = y$:

$$\underbrace{-\overline{\rho u_x u_y \Psi}}_{\tau_R} \underbrace{+2\overline{\mu S_{xy}\Psi}}_{\tau_V} \underbrace{-\overline{\rho u_x u_y\,(1-\Psi)}}_{\tau_M} \underbrace{+\left\{2\overline{\mu S_{xy}\,(1-\Psi)} + \int_0^y \overline{F_x}(y')\,\mathrm{d}y'\right\}}_{\tau_S} = \tau. \tag{B 1c}$$

The total shear stress τ is decomposed into four terms. The first term is stress due to liquid velocity fluctuations τ_R, referred to as liquid Reynolds stress. The second term is stress due to liquid viscosity τ_V, referred to as liquid viscous stress. The third term is stress due to particle velocity fluctuations τ_M, referred to as particle momentum flux. The fourth term is due to stresses on the particle surfaces τ_S, referred to as particle surface stress. The right-hand side represents the wall shear stress $\tau_W = 2\mu\overline{S_{xy}}|_{y=0}$. In fully developed Couette flow the sum of all stresses τ is independent of y and equal to τ_W.

REFERENCES

Benzi, R., Ching, E. S. C., De Angelis, E. & Procaccia, I. 2008 Comparison of theory and direct numerical simulations of drag reduction by rodlike polymers in turbulent channel flows. *Phys. Rev.* E **77**, 046309.

Benzi, R., Ching, E. S. C., Lo, T. S., L'vov, V. S. & Procaccia, I. 2005 Additive equivalence in turbulent drag reduction by flexible and rodlike polymers. *Phys. Rev.* E **72** (1), 016305.

Chen, M., Kontomaris, K. & McLaughlin, J. B. 1998 Direct numerical simulation of droplet collisions in a turbulent channel flow. Part I. Collision algorithm. *Intl J. Multiphase Flow* **24**, 1079–1103.

De Angelis, E., Casciola, C. M., L'vov, V. S., Pomyalov, A., Procaccia, I. & Tiberkevich, V. 2004 Drag reduction by a linear viscosity profile. *Phys. Rev.* E **70** (5), 055301.

https://doi.org/10.1017/jfm.2012.510 Published online by Cambridge University Press

GILLISSEN, J. J. J., BOERSMA, B. J., MORTENSEN, P. H. & ANDERSSON, H. I. 2007 The stress generated by non-Brownian fibres in turbulent channel flow simulations. *Phys. Fluids* **19** (11), 115107.

GILLISSEN, J. J. J., SUNDARESAN, S. & VAN DEN AKKER, H. E. A. 2011 A lattice Boltzmann study on the drag force in bubble swarms. *J. Fluid Mech.* **679**, 101–121.

GUST, G. 1976 Observations on turbulent-drag reduction in a dilute suspension of clay in sea-water. *J. Fluid Mech.* **75** (1), 29–47.

IACCARINO, G., SHAQFEH, E. S. G. & DUBIEF, Y. 2010 Reynolds-averaged modelling of polymer drag reduction in turbulent flows. *J. Non-Newtonian Fluid Mech.* **165** (7–8), 376–384.

KOMMINAHO, J., LUNDBLADH, A. & JOHANSSON, A. V. 1996 Very large structures in plane turbulent Couette flow. *J. Fluid Mech.* **320**, 259–285.

LU, J., FERNÁNDEZ, A. & TRYGGVASON, G. 2005 The effect of bubbles on the wall drag in a turbulent channel flow. *Phys. Fluids* **17** (9), 095102.

LUMLEY, J. L. 1973 Drag reduction in turbulent flow by polymer additives. *J. Polym. Sci. Macromol. Rev.* **7** (1), 263–290.

MADAVAN, N. K., DEUTSCH, S. & MERKLE, C. L. 1985 Measurements of local skin friction in a microbubble-modified turbulent boundary layer. *J. Fluid Mech.* **156**, 237–256.

MCCOMB, W. D. & CHAN, K. T. J. 1985 Laser–Doppler anemometer measurements of turbulent structure in drag-reducing fibre suspensions. *J. Fluid Mech.* **152**, 455–478.

PASINATO, H. D. 2011 Velocity and temperature dissimilarity in fully developed turbulent channel and plane Couette flows. *Intl J. Heat Fluid Flow* **32** (1), 11–25.

RASHIDI, M., HETSRONI, G. & BANERJEE, S. 1990 Particle-turbulence interaction in a boundary layer. *Intl J. Multiphase Flow* **16** (6), 935–949.

TAYLOR, G. I. 1932 The viscosity of a fluid containing small drops of another fluid. *Proc. R. Soc. Lond.* A **138**, 41–48.

UHLMANN, M. 2005 An immersed boundary method with direct forcing for the simulation of particulate flows. *J. Comput. Phys.* **209** (2), 448–476.

VIRK, P. S. 1975 Drag reduction fundamentals. *AIChE J.* **21** (4), 625–656.

WARHOLIC, M. D., MASSAH, H. & HANRATTY, T. J. 1999*a* Influence of drag-reducing polymers on turbulence: effects of Reynolds number, concentration and mixing. *Exp. Fluids* **27**, 461–472.

WARHOLIC, M. D., SCMHIDT, G. M. & HANRATTY, T. J. 1999*b* The influence of a drag-reducing surfactant on a turbulent velocity field. *J. Fluid Mech.* **388**, 1–20.

WOLF-GLADROW, D. A. 2000 *Lattice-Gas Cellular Automata and Lattice Boltzmann Models. An Introduction*. Springer.

XI, L. & GRAHAM, M. D. 2010 Turbulent drag reduction and multistage transitions in viscoelastic minimal flow units. *J. Fluid Mech.* **647**, 421–452.

XU, J., MAXEY, M. R. & KARNIADAKIS, G. E. 2002 Numerical simulation of turbulent drag reduction using micro-bubbles. *J. Fluid Mech.* **468**, 271–281.

ZHAO, L. H., ANDERSSON, H. I. & GILLISSEN, J. J. J. 2010 Turbulence modulation and drag reduction by spherical particles. *Phys. Fluids* **22** (8), 081702.

https://doi.org/10.1017/jfm.2012.510 Published online by Cambridge University Press